



PCCP

**Impact of Sodium Vanadium Oxide (NaV_3O_8 , NVO) Material
Synthesis Conditions on Charge Storage Mechanism in Zn-
ion Aqueous Batteries**

Journal:	<i>Physical Chemistry Chemical Physics</i>
Manuscript ID	CP-ART-02-2021-000516.R1
Article Type:	Paper
Date Submitted by the Author:	16-Mar-2021
Complete List of Authors:	Tang, Christopher; Stony Brook University, Singh, Gurpreet; Stony Brook University, Chemistry Housel, Lisa; Stony Brook University Kim, Sung Joo; Brookhaven National Laboratory, Interdisciplinary Science Quilty, Calvin; Stony Brook University, Department of Chemistry Zhu, Yimei; Brookhaven National Laboratory Wang, Lei; Brookhaven National Laboratory, Energy and Photon Science Takeuchi, Kenneth; Stony Brook University, Chemistry Takeuchi, Esther; Stony Brook University, Materials Science and Engineering Marschilok, Amy; Stony Brook University, Chemistry

SCHOLARONE™
Manuscripts

Impact of Sodium Vanadium Oxide (NaV₃O₈, NVO) Material Synthesis Conditions on Charge Storage Mechanism in Zn-ion Aqueous Batteries

[†]Christopher R. Tang^{1,2}, [‡]Gurpreet Singh^{1,3}, [‡]Lisa M. Housel^{1,4}, Sung Joo Kim^{4,5}, Calvin D. Quilty^{1,3}, Yimei Zhu^{4,5}, Lei Wang^{1,4}, Kenneth J. Takeuchi^{1,3*}, Esther S. Takeuchi^{1,2,3,4*}, Amy C. Marschilok^{1,2,3,4*}

¹Institute for Electrochemically Stored Energy, State University of New York at Stony Brook, Stony Brook, New York 11794, United States

²Department of Materials Science and Chemical Engineering, Stony Brook University, Stony Brook, New York 11794, United States

³Department of Chemistry, Stony Brook University, Stony Brook, New York 11794, United States

⁴Interdisciplinary Science Department, Brookhaven National Laboratory, Upton, New York 11973, United States

⁵Condensed Matter Physics and Materials Science Department, Brookhaven National Laboratory, Upton, New York 11973, United States

⁶Department of Physics and Astronomy, Stony Brook University, Stony Brook, New York 11794, United States

[†]contributed equally to the manuscript

*corresponding authors: (K.J.T.) kenneth.takeuchi.1@stonybrook.edu, (E.S.T.) esther.takeuchi@stonybrook.edu, (A.C.M.) amy.marschilok@stonybrook.edu

Abstract

The electrochemical charge storage of sodium vanadate (NaV₃O₈ or NVO) cathodes in aqueous Zn-ion batteries has been hypothesized to be influenced by the inclusion of structural water for facilitating ion transfer in the material. Materials properties considered important (morphology, crystallite and particle size, surface area) are systematically studied herein through investigation of two NVO materials, NaV₃O₈·0.34H₂O [NVO(300)] and NaV₃O₈·0.05H₂O [NVO(500)], with different water content, acicular morphologies with different size and surface area achieved via post-synthesis heat treatment. The electrochemistry of the two materials was evaluated in aqueous Zn-ion cells with 2 M ZnSO₄ electrolyte using cyclic voltammetry, galvanostatic cycling, and rate capability testing. The thinner NVO(300) nanobelts (0.13 μm) demonstrate greater specific capacities and higher effective diffusion coefficients relative to the thicker NVO(500) nanorods. Notably however, while cells containing NVO(500) deliver lower specific capacity, they demonstrate enhanced capacity retention with cycling. The structural changes accompanying oxidation and reduction are elucidated via *ex-situ* x-ray diffraction, transmission electron microscopy, and *operando* V K-edge x-ray absorption spectroscopy (XAS), where NVO material properties are shown to influence the ion insertion. *Operando* XAS verified that electron transfer corresponds directly to change in vanadium oxidation state, affirming vanadium redox as the governing electrochemical process.

Introduction

Implementation of intermittent renewable energy sources derived from wind and solar power motivates development of safe, sustainable, low cost energy storage devices, specifically batteries based on aqueous electrolytes. Zn has a high theoretical capacity (820 mAh/g), low redox potential (-0.76 V vs. SHE), and low toxicity such that aqueous electrolyte zinc based batteries may prove to be a desirable alternative for Li-ion batteries for some applications.^{1,2}

Vanadium based materials are appealing for aqueous electrochemical energy storage due to the multiple accessible redox states for the vanadium center.³⁻⁹ Layered vanadates, supported by cation pillars, are of interest for Zn-ion batteries as the vanadium redox center allows for high capacity and the layered structure promotes facile ion transfer.¹⁰⁻¹² In particular, sodium vanadium oxides (NVO) show promise as cathode materials for Zn-ion aqueous batteries.¹³⁻²² Notably, the electrochemistry and subsequent charge storage mechanism can be highly dependent on the material properties of NVO, where structural hydration,^{16, 17, 22} morphology,¹² size,²² and host-ion valence¹⁷ can influence ion transport within the vanadate layers.

Recently, the influence of NVO hydration on the electrochemistry of Zn-ion aqueous cells has been investigated.^{15, 17, 21, 23, 24} For example, hydrated $\text{Na}_2\text{V}_6\text{O}_{16} \cdot 1.63 \text{H}_2\text{O}$ demonstrates superior capacity retention and delivered specific capacities relative to the dehydrated NaV_3O_8 in $\text{Zn}(\text{CF}_3\text{SO}_3)_2$ aqueous electrolyte.²³ Notably, $\text{Na}_2\text{V}_6\text{O}_{16} \cdot 1.63 \text{H}_2\text{O}$ delivered 352 mAh/g at 50 mA/g with capacity retention of 90% after 6000 cycles at 5 A/g.²³ In contrast, the delivered capacity of NaV_3O_8 cells decreased from 120 mAh/g to 20 mA/g after 4000 cycles, resulting in a capacity retention of 17%.²³ Similar conclusions were drawn for NVO cells with 2 M ZnSO_4 electrolyte, where non-hydrated $\text{Na}_{1.25}\text{V}_3\text{O}_8$ delivered lower initial specific capacities [126 mAh/g], but demonstrated improved capacity retention [90% after 50 cycles at 200 mA/g] relative to hydrated $\text{Na}_2\text{V}_6\text{O}_{16} \cdot 2\text{H}_2\text{O}$ [190 mAh/g; 74% capacity retained after 50 cycles at 200 mA/g].¹⁵

Reversible or partially reversible Zn^{2+} insertion/extraction in both hydrated and non-hydrated NVO materials during discharge/charge has been reported using bulk and local techniques. Decreases in the (001) d-spacing have been observed after discharge using x-ray diffraction and are attributed to strong electrostatic interaction between Zn^{2+} and V_3O_8 layers.^{17, 19} *Ex situ* solid-state ^1H nuclear magnetic resonance (NMR) and Zn 2p x-ray photoelectron spectroscopy (XPS) measurements have suggested H^+ and Zn^{2+} co-insert into the NVO structure on discharge.²⁰ Additionally, *ex-situ* XPS and x-ray near edge absorption spectroscopy (XANES) measurements have suggested Zn^{2+} and/or H^+ insertion corresponds to decreases in the vanadium oxidation state.^{19, 22, 25} The formation of zinc hydroxyl sulfate ($\text{Zn}_4\text{SO}_4(\text{OH})_6 \cdot x\text{H}_2\text{O}$) and partially reversible Zn-inserted vanadium oxide phases on discharge are also frequently reported.^{15, 19, 20, 22}

Understanding the key parameters that govern the charge storage mechanism of the Zn/NVO aqueous systems remains a critical challenge.¹⁵ Investigations that probe mechanism by tuning material properties can provide a pathway for ultimately controlling electrochemical outcomes in Zn/NVO systems. For example, recent transmission electron microscopy (TEM), energy dispersive spectroscopy (EDS), and electron energy loss spectroscopy (EELS) analyses indicated

that Zn (de)insertion depended on both the presence of crystal water in the interlayer and thickness of the nanostructures.¹⁵ The lower discharge capacity of the thick (120-170 nm), dehydrated $\text{Na}_{1.25}\text{V}_3\text{O}_8$ material was attributed to a surface-limited Zn redox reaction. In contrast, the thin (30-50 nm), hydrated $\text{Na}_2\text{V}_6\text{O}_{16}\cdot 2\text{H}_2\text{O}$ material facilitated greater Zn insertion for the bulk structure, resulting in higher specific capacities.¹⁵

This work demonstrates the influence of material properties on the electrochemistry of NVO in Zn-ion aqueous cells. The properties of NVO were controlled through post synthesis heat treatment of the material to produce two NVO materials, $\text{NaV}_3\text{O}_8\cdot 0.34\text{H}_2\text{O}$ [NVO(300)] and $\text{NaV}_3\text{O}_8\cdot 0.05\text{H}_2\text{O}$ [NVO(500)]. The impacted material properties considered include water content, lattice parameters, particle and crystallite size, morphology, and surface area. The effects of these properties on the electrochemistry on both materials was investigated, providing implications for controlling electrochemical properties through modification of synthesis conditions.

Experimental

Material synthesis and characterization: The synthesis of NVO(300) and NVO(500) was adapted from a previously reported sol gel process.²⁶ Briefly, a hydrated precursor was annealed in air for 3 hours at 300°C for NVO(300) or 500°C for NVO(500). Water content was determined using a TA Q500 thermogravimetric analysis (TGA) instrument. Surface area was measured via the Brunauer–Emmett–Teller (BET) method using a Quantachrome 4200E. Elemental composition ratios of Na:V were measured by a Thermo Scientific iCAP 6000 inductively coupled plasma-optical emission spectrometer (ICP-OES). Powder x-ray diffraction was acquired at Beamline 28-ID-2 (XPD) of the National Synchrotron Light Source-II (NSLS-II) at Brookhaven National Laboratory. The beamline was calibrated ($\lambda = 0.19167 \text{ \AA}$) using a LaB₆ standard. Rietveld refinement was conducted using GSAS-II software.²⁷ NVO(500) was refined using an anhydrous Na_xV₃O₈ starting structure.²⁸ NVO(300) was refined by introducing interlayer water to the anhydrous Na_xV₃O₈ structure in 2e sites (x, 1/4, z).²⁹ Scanning electron microscopy (SEM) images of NVO materials were acquired using a JEOL-7600F instrument at an accelerating voltage of 10kV. Particle size distribution was determined using ImageJ software where 30 particles of each NVO material were chosen for analysis.³⁰

Electrochemical methods: NVO and carbon nanotubes (CNT) powders were dispersed in ethanol via sonication bath and vacuum filtered to fabricate thick porous electrodes with a mass ratio of 7:3 (NVO:CNT). Electrochemical tests were performed in stainless steel coin cells with the NVO/CNT cathode, glass fiber separator, Zn foil anode, and 2 M ZnSO₄ aqueous electrolyte. Galvanostatic cycling and rate capability testing were performed using a Maccor battery tester at 30°C. Cyclic voltammetry was collected using a BioLogic VSP multichannel potentiostat.

Post Cycling Characterization:

Ex-situ XRD of the NVO/CNT electrodes before and after cycle 1 (dis)charge at 50 mA/g were collected at Beamline 28-ID-2 (XPD) of NSLS-II at Brookhaven National Laboratory. The beamline was calibrated ($\lambda = 0.19167 \text{ \AA}$) using a LaB₆ standard. Rietveld refinement was conducted using GSAS-II software.²⁷

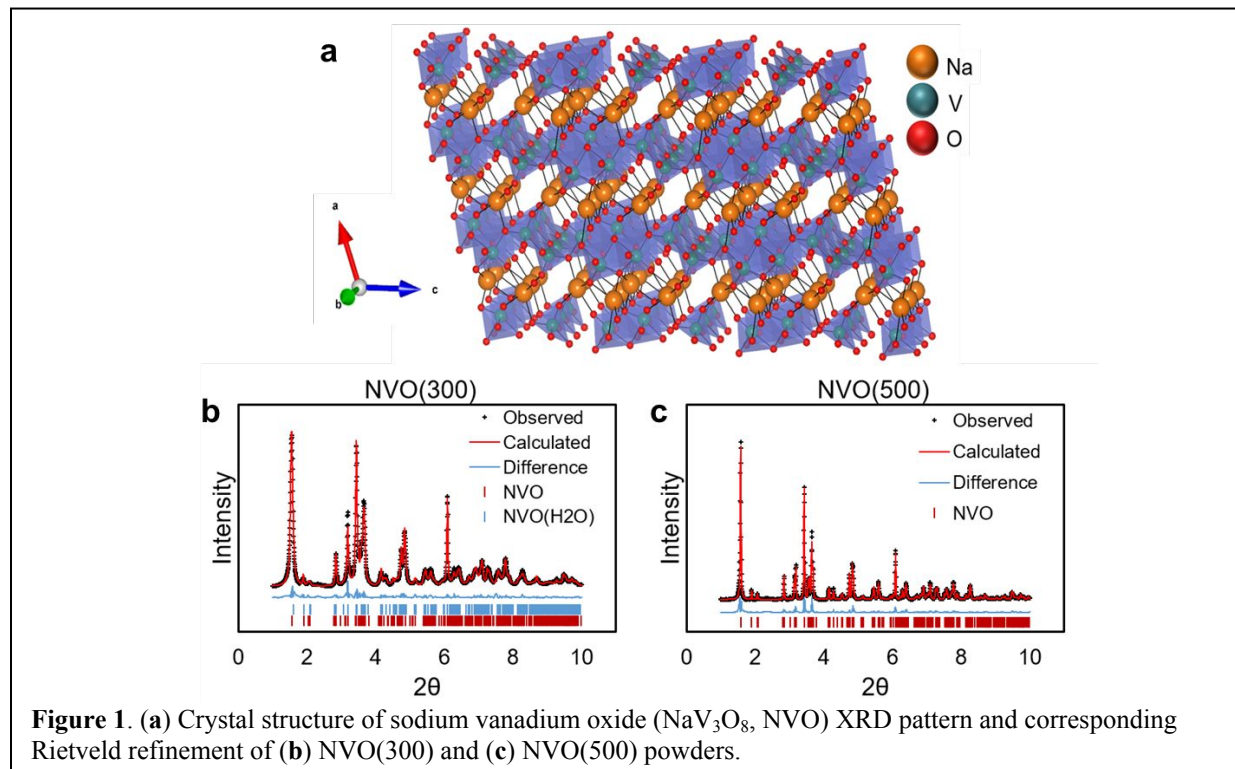
Transmission electron microscope (TEM) images and selected area electron diffraction (SAED) patterns of pristine, discharged, and charged NVO were obtained using a JEOL ARM 200CF microscope, operated at 200 kV, equipped with double spherical aberration correctors (CEOS GmbH) and GIF Quantum ER Energy Filter (Gatan). Scanning TEM (STEM) imaging and energy dispersive spectroscopy (EDS) mapping were performed using an Oxford Energy TEM 250 spectrometer inside a JEOL-JEM 2100F microscope operating at 200 kV.

Fluorescence-mode *operando* X-ray absorption spectroscopy (XAS) measurements were collected at the vanadium K edge at the NIST Beamline for Materials Measurement (BMM, 6-BM) of NSLS-II at Brookhaven National Laboratory. *Operando* cells were constructed with NVO/CNT cathode, Zn foil anode, glass fiber separator, and 2 M ZnSO₄ electrolyte. NVO(300), NVO(500), V₂O₅, VO₂, and V₂O₃ powdered standards were mixed with boron nitride and pressed into pellets prior to measurement. All XAS transmission and fluorescence spectra were background subtracted (Rbkg = 1.0), aligned, merged, and normalized by using Athena from the Demeter software

package.^{31, 32} The edge position of the normalized XAS spectra was estimated at 50% of the edge jump intensity.

Results

Material characterization



NaV_3O_8 synthesized via a sol-gel reaction and heated at 300°C or 500°C produced the NVO(300) and NVO(500) materials, respectively. The NaV_3O_8 layered structure is comprised of stacked VO_5 square-pyramids and edge-sharing VO_6 octahedra along the (100) axis (Figure 1a).³³ Na cations are located in octahedral sites between the V_3O_8 layers where the interlayer spacing can be affected by the ionic radius of the intercalated ions and water content. For anhydrous and monohydrated phases of NaV_3O_8 , the calculated average interlayer V-V distance along the (100) plane is ~ 5.39 Å and 5.46 Å, respectively.

X-ray diffraction patterns of the NVO(300) (Figure 1b) and NVO(500) (Figure 1c) materials collected using synchrotron radiation were fit using Rietveld refinement. NVO(500) was successfully fit using the anhydrous reference; whereas, the NVO(300) pattern was fit using both the anhydrous and monohydrated references.^{28, 29} The refined lattice parameters, crystallite size, and microstrain for NVO(300) and NVO(500) are summarized in Table S1. The refined Na, V, and O atomic positions are summarized in Table S2 and Table S3 for NVO(300) and NVO(500), respectively. For NVO(500), the refined unit cell parameters were: $a = 0.73$, $b = 0.36$, $c = 1.22$ nm, $\beta = 107.8^\circ$, and $V = 0.306$ nm³ ($R_{\text{wp}} = 8.3\%$). The NVO(300) powder consisted of anhydrous (24%) and monohydrate (76%) phases. The refined anhydrous/monohydrate phase unit cell parameters for NVO(300) are: $a = 0.73/0.72$ nm, $b = 0.36/0.36$ nm, $c = 1.21/1.22$ nm, $\beta = 106.8/107.7^\circ$, and $V = 0.311/0.303$ nm³ ($R_{\text{wp}} = 6.0\%$). Note that the fit for the refinement was

significantly improved when considering the material with both the hydrated and non-hydrated parent structures. The refined axial (100) crystallite sizes for NVO(300) and NVO(500) were 17/19 nm (anhydrous/hydrated) and 61 nm, respectively. The smaller crystallite size for the NVO(300) material is consistent with the observed intensity decrease and broadening of the peaks throughout the XRD pattern relative to the NVO(500) material. Interlayer spacing (*a*-plane) calculated from the position of the (100) peak were 7.06 Å and 6.98 Å for NVO(300) and NVO(500), respectively. Consistent unit cell parameters and atomic positions indicate that the annealing alters crystallite size and *a*-plane interlayer spacing without significant change to the NVO crystal structure.

ICP-OES identified the Na:V ratio as 1:3, indicating a stoichiometry of NaV_3O_8 . Thermogravimetric analysis (TGA) was performed to determine water content (**Figure S1**). The water contents of the hydrated NVO precursor, NVO(300), and NVO(500) materials were 8.6 %, 2.0 %, and 0.5 % respectively. These percentages correspond to a chemical composition of $\text{NaV}_3\text{O}_8 \cdot x\text{H}_2\text{O}$, where *x* is 1.59, 0.34, and 0.05 for the hydrated NVO precursor, NVO(300) and NVO (500) materials, respectively, where the annealed materials show significantly less water than the hydrated precursor. BET analysis indicated a change in surface area upon annealing, starting with 35 m²/g for the hydrated precursor, and resulting in 18 m²/g for NVO(300), and 4 m²/g for NVO(500). The decrease in surface area with annealing temperature is consistent with the observed increase in crystallite size from XRD.

SEM images reveal NVO(300) (**Figure 2a – c**) and NVO(500) (**Figure 2d – f**) have acicular morphologies with different particle sizes. The dimensions of the NVO materials were determined by averaging the length and width of 30 selected particles from the SEM images (**Figures S2a, S2b**). The average length of the NVO(300) nanobelts is $2.8 \pm 0.7 \mu\text{m}$ and the average width is $0.13 \pm 0.04 \mu\text{m}$ where the nanobelts appear flexible and are intertwined. In contrast, NVO(500) (**Figure 2d – e**) has a thicker nanorod morphology with an average length of $3.6 \pm 1.2 \mu\text{m}$, an average width of $0.29 \pm 0.10 \mu\text{m}$, and appears rigid relative to the NVO(300) nanobelts. The larger particle size of the NVO(500) nanorods is attributed to the higher annealing temperature.

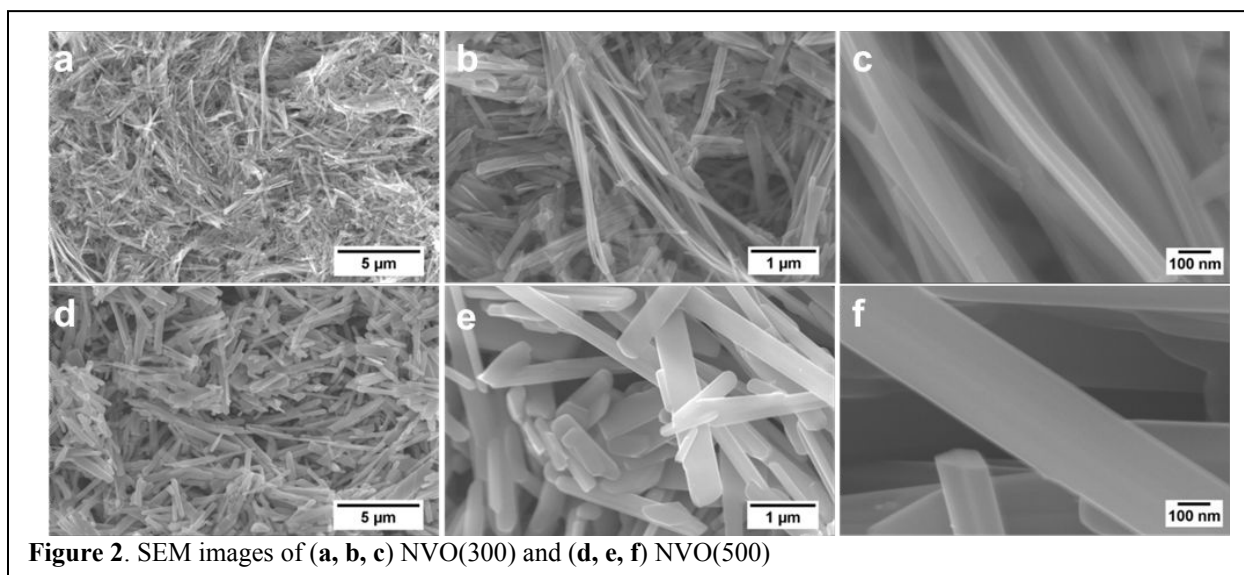


Figure 2. SEM images of (a, b, c) NVO(300) and (d, e, f) NVO(500)

Transmission electron microscopy (TEM) and selected area electron diffraction (SAED) of representative as-synthesized NVO(300) and NVO(500) powders are shown in **Figure 3**. NVO(300) exhibits slab-like or nanobelt morphology while NVO(500) has rod-like morphology (**Figure 3a and d**). SAED patterns confirm high crystallinity of both nanostructures (**Figure 3c and f**). The measured *c*-plane spacing of NVO(300) and NVO(500) are ~ 1.18 and 1.16 nm consistent with a previous literature report.²⁶ The slightly increased interlayer spacing suggests NVO(300) has slightly higher water content located within the layers, consistent with TGA results and XRD, where refinements required inclusion of the monohydrated phase.

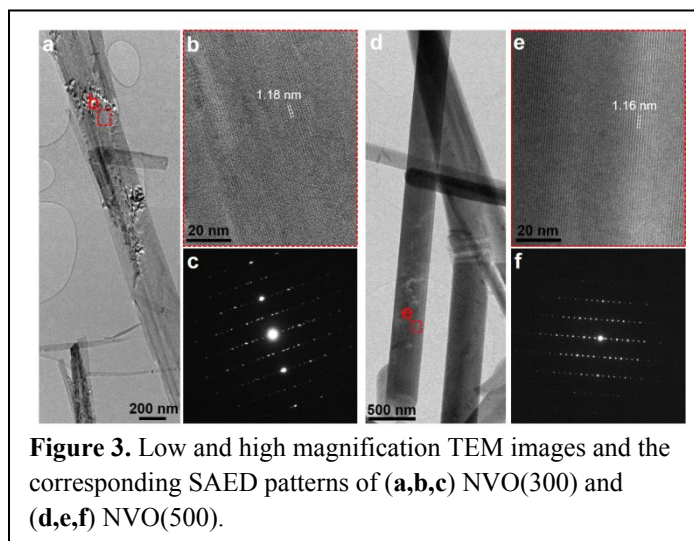


Figure 3. Low and high magnification TEM images and the corresponding SAED patterns of (a,b,c) NVO(300) and (d,e,f) NVO(500).

The XRD, TEM, and SEM results confirm that two different crystallite size materials were obtained by altering the annealing temperature of the hydrated precursor. In addition to crystallite size, NVO(300) and NVO(500) have acicular morphologies with distinct particle size and surface area, indicated by SEM, and BET, respectively. Notably, TGA, XRD, and TEM also indicate NVO(300) has higher water content in the interlayer spacing.

Electrochemistry

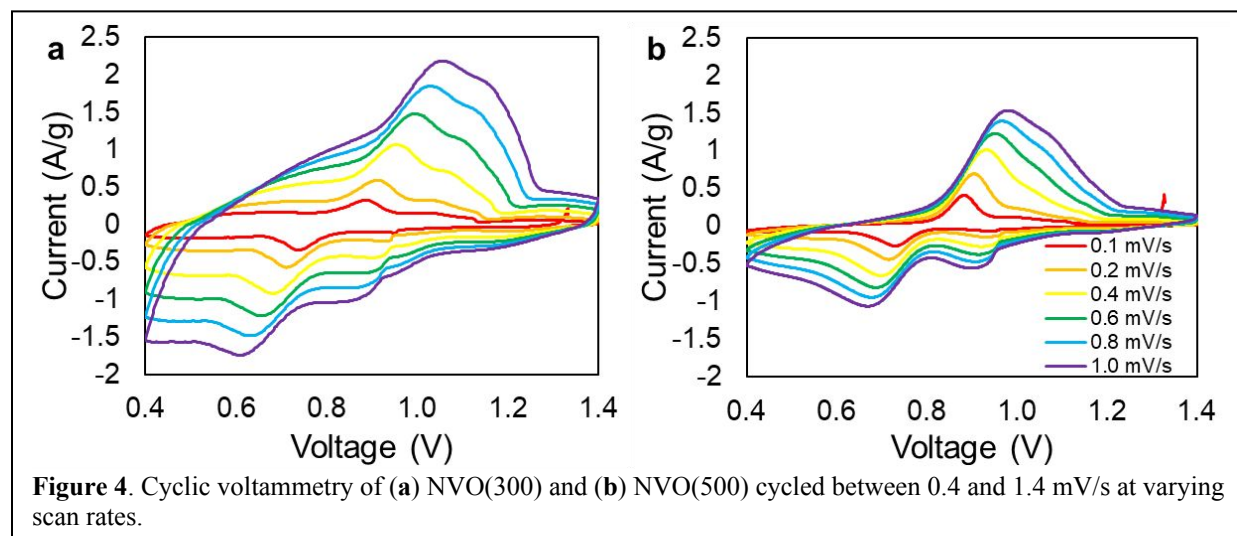


Figure 4. Cyclic voltammetry of (a) NVO(300) and (b) NVO(500) cycled between 0.4 and 1.4 V at varying scan rates.

The electrochemical differences between NVO(300) and NVO(500) were analyzed using cyclic voltammetry (CV) versus Zn/Zn^{2+} at a series of scan rates with 2 M ZnSO_4 electrolyte (**Figure 4**). The NVO(300) and NVO(500) materials were cycled 20 times at 1 A/g prior to CV measurements to ensure a stable electrochemistry. Both NVO(300) and NVO(500) exhibit two redox couples in their voltammograms. The measured peak currents during the two redox couples are larger for

NVO(300) relative to NVO(500). Peak potentials, peak-to-peak separation distances, and $E_{1/2}$ values for the first and second redox couple are summarized in **Tables S4** and **Table S5**.

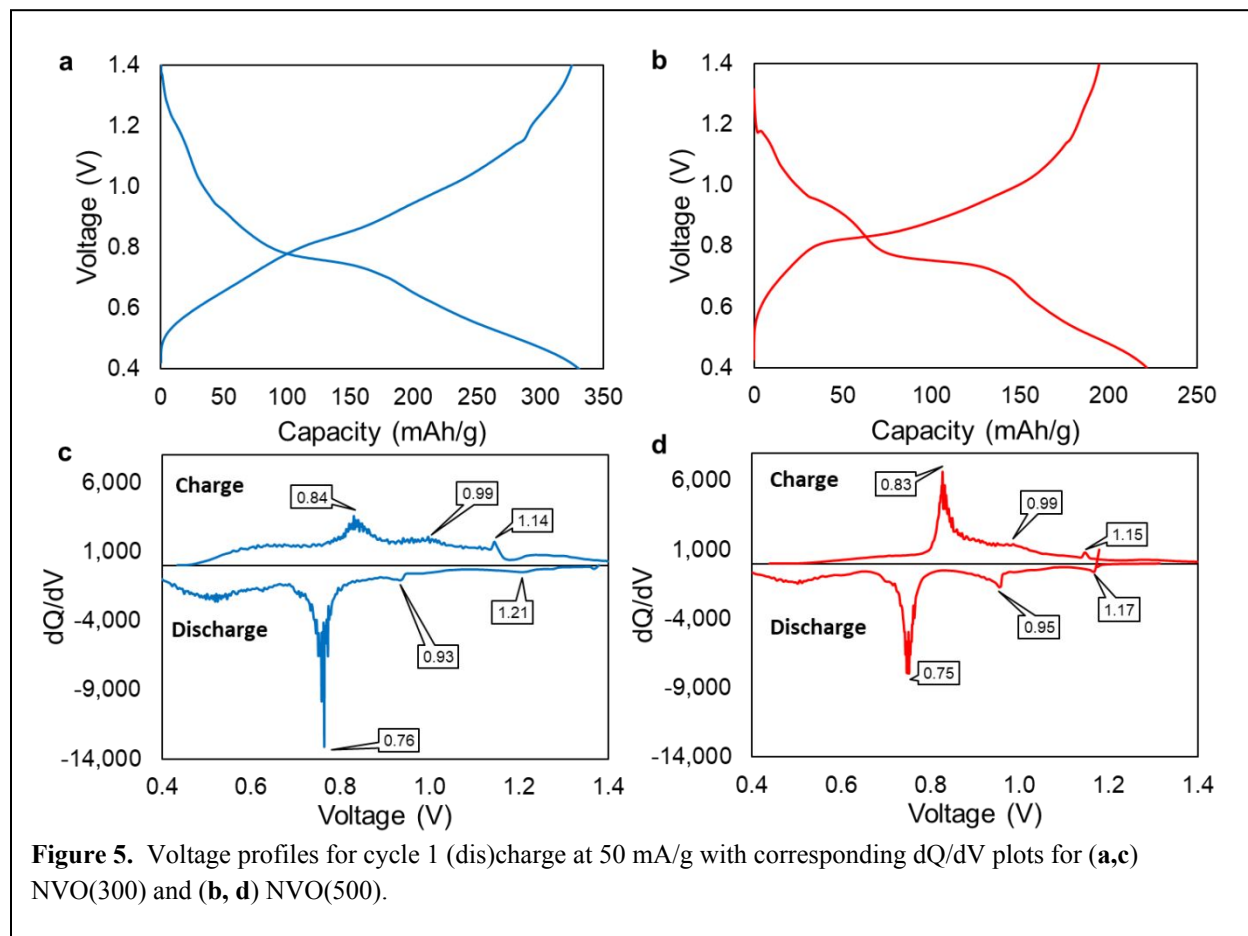
For NVO(300), the cathodic/anodic peak potentials of the first and second redox couple are 0.88 V/1.02 V and 0.74 V/0.89 V, respectively at 0.1 mV/s. At 1.0 mV/s, the cathodic peak potential shifts negatively and the anodic peak potential shifts positively, resulting in an increased peak-to-peak (ΔE) separation as a function of increasing scan rate. From 0.1 mV/s to 1.0 mV/s, the $E_{1/2}$ value shifts slightly from 0.81 V to 0.83 V. The NVO(500) cell shows two similar, yet more distinct redox couples (**Figure 4b**). At 0.1 mV/s, the first cathodic peak appears at 0.95 V with the corresponding anodic peak at 0.98 V. The second redox peaks are present at 0.73 V and 0.89 V in the cathodic and anodic scans, respectively. The NVO(500) cell also exhibits an increase in ΔE as function of increasing scan rate and a shift in $E_{1/2}$ from 0.81 V to 0.83 V.

The diffusion coefficients of NVO(300) and NVO(500) were estimated from the second and major redox couple using the Randles-Sevcik equation (**Equation 1**),

$$i_p = 0.4463nFAC\left(\frac{nFvD}{RT}\right)^{1/2} \quad (1)$$

where i_p is the peak current, n is the number of electrons transferred, F is Faraday's constant, A is the electrode area, C is the concentration, v is the scan rate, D is the diffusion coefficient, R is the gas constant, and T is the temperature. The peak currents show a linear dependence on the square root of the scan rate for both NVO(300) and NVO(500), suggesting a diffusion-controlled process for the redox event (**Figure S3**). The slopes of the NVO(300) Randles-Sevcik plots upon reduction (**Figure S3a**) and oxidation (**Figure S3b**) were $3.1\text{E-}4$ and $4.16\text{E-}4$ $\text{As}^{1/2}/\text{mV}^{1/2}$, respectively. In comparison, slopes for NVO(500) were lower on reduction and oxidation at $1.7\text{E-}4$ $\text{As}^{1/2}/\text{mV}^{1/2}$ (**Figure S3c**) and $2.2\text{E-}4$ $\text{As}^{1/2}/\text{mV}^{1/2}$ (**Figure S3d**), respectively. The steeper slopes for the NVO(300) nanobelt electrodes indicate a larger effective diffusion coefficient relative to the NVO(500) nanorod electrodes, consistent with greater surface area, thinner particle morphology and greater interlayer distance.

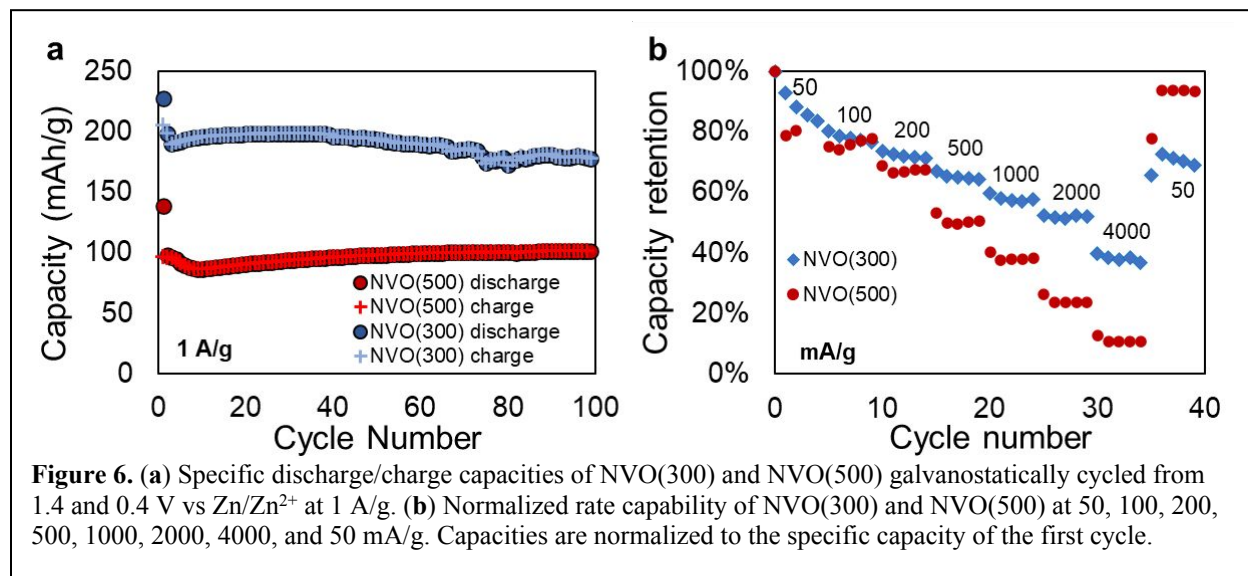
NVO(300) and NVO(500) electrodes were evaluated through galvanostatic testing. The first cycle discharge profile at 50 mA/g for NVO(300) (**Figure 5a**) exhibits two short plateaus at 1.21 V and 0.93 V and a longer plateau at 0.76 V. Three charge plateaus are also present at 0.84 V, 0.99 V, and 1.14 V. Similar voltage plateaus are present for NVO(500) during cycle 1 discharge (1.17, 0.95, and 0.75 V) and charge (0.83, 0.99, and 1.15 V) (**Figure 5b**). During the first discharge, NVO(300) delivers 330 mAh/g and NVO(500) delivers 221 mAh/g. During the first charge, NVO(300) recovers 324 mAh/g and NVO(500) recovers 195 mAh/g. The distinct features in the voltage profile are more easily identified via differential capacity (dQ/dV) profiles (**Figure 5c, 5d**) reminiscent of the CV results.



Zn/NVO cells were cycled between 0.4 and 1.4 V for 100 cycles at 1 A/g (**Figure 6a**). NVO(300) delivers initial discharge and charge capacities of 228 mAh/g and 205 mAh/g, respectively, corresponding to a Coulombic efficiency of 90%. During cycle 2, the delivered capacity decreases to 199 mAh/g on discharge and charge. The capacity reaches 177 mAh/g by cycle 100. The NVO(500) cell delivers a lower capacity on first discharge (139 mAh/g) and has a lower Coulombic efficiency (70%) than NVO(300). NVO(500) discharge capacity decreases to 98 mAh/g by cycle 2 and reaches a minimum at cycle 9 (86 mAh/g). At cycle 100, the NVO(500) cell delivers 101 mAh/g, representing a 3% increase to the capacity relative to cycle 2. From the long-term cycling data, NVO(300) delivers higher (dis)charge capacities at each cycle, yet experiences a 10% capacity fade after 100 cycles relative to the second cycle in contrast to the NVO(500) sample. Notably, both NVO(300) and NVO(500) cells experience a low Coulombic efficiency in cycle 1, consistent with partially irreversible Zn-intercalation into the NVO lattice noted in previous reports.^{17, 20, 26} Cycle 100 Coulombic efficiencies were 99.6% and 99.9% for NVO(300) and NVO(500), respectively.

The rate capability for NVO(300) and NVO(500) was evaluated at current densities of 50, 100, 200, 500, 1000, 2000, 4000, and with return to 50 mA/g for five cycles at each rate (**Figure 6b**). At lower rates (50, 100, and 200 mA/g), the NVO(300) and NVO(500) cells demonstrate comparable normalized capacity retention. At 500, 1000, 2000, and 4000 mA/g, NVO(300) has a delivered capacity 15, 19, 28, 27% higher than NVO(500). Upon returning to 50 mA/g, NVO(500)

exhibits an overall capacity retention of 93%; whereas, the capacity retention for NVO(300) is 69% based on the capacity fade during the 40 cycles. The improved rate capability of NVO(300) compared to NVO(500) is consistent with the larger effective diffusion coefficients for NVO(300) determined from the cyclic voltammetry results.

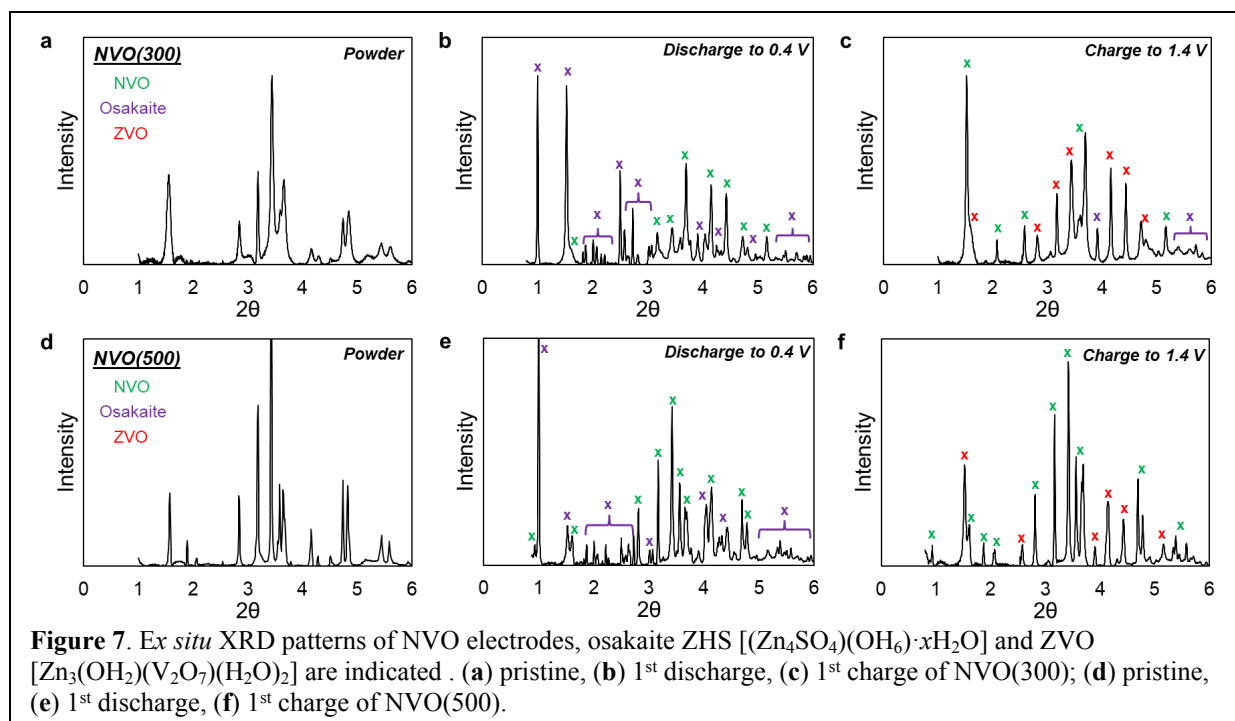


Cycling and rate capability testing indicate that NVO(300) delivers higher capacity, but experiences greater capacity decrease with extended cycling. Moreover, the higher capacity of NVO(300) at higher rates is consistent with cyclic voltammetry results, which indicate NVO(300) has improved diffusion relative to NVO(500). Thus, cyclic voltammetry and rate capability tests indicate that the ion transfer is more facile in NVO(300). Long term cycling shows NVO(300) can accommodate more charge relative to NVO(500), which can result in greater structural change and a decrease in long term cycling stability. Additionally, the longer cycling time of NVO(300) may increase vanadium dissolution, which can contribute to capacity fade in this system.^{18, 20, 26}

These electrochemical observations are consistent with the smaller crystallite size, thinner morphology, higher surface area, and slightly larger interlayer spacing of the NVO(300) material.

Post-Electrochemistry Characterization

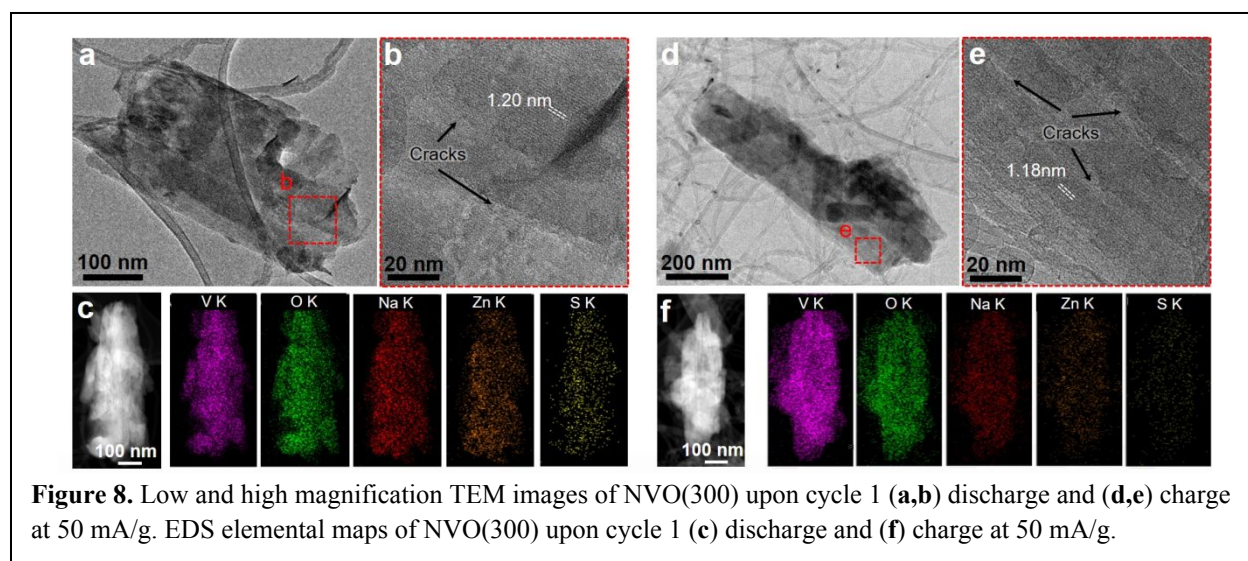
Ex-situ Characterization XRD



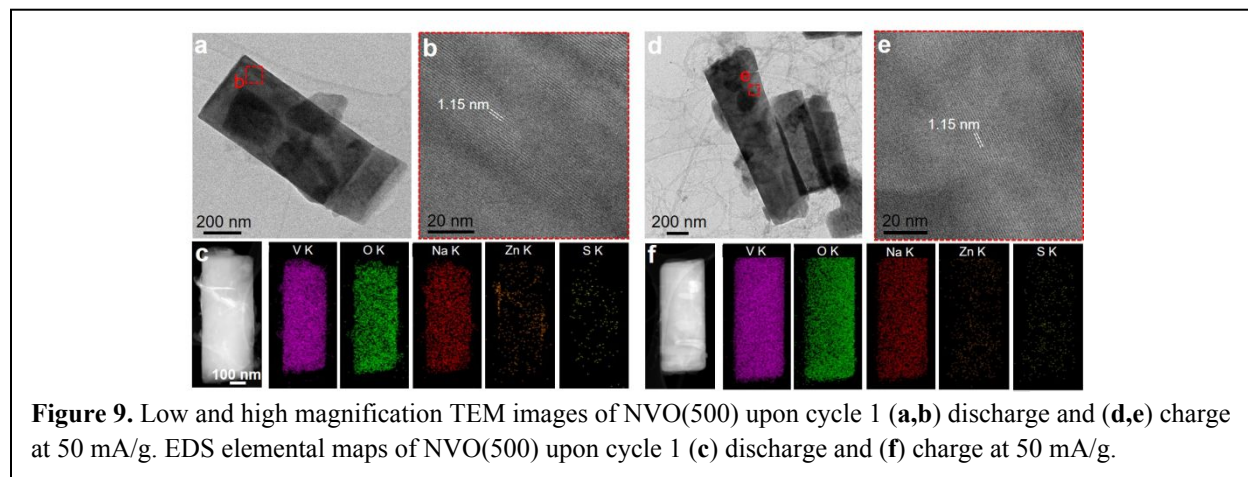
XRD was collected on recovered NVO(300) and NVO(500) electrodes after discharge to 0.4 V and after charge to 1.4 V vs Zn/Zn^{2+} at 50 mA/g (**Figure 7**). Rietveld refinement of the discharged NVO(300) electrode indicates the presence of the anhydrous and hydrated NVO, $\text{Zn}_4\text{SO}_4(\text{OH})_6 \cdot 5\text{H}_2\text{O}$ (ZHS – PDF# 00-039-0688) and zinc vanadium oxide $\text{Zn}_3(\text{OH})_2\text{V}_2\text{O}_7 \cdot 2\text{H}_2\text{O}$, (ZVO – PDF# 00-050-0570) phases (**Figure 7b**, **Figure S4a**). The phase composition of the NVO(300) discharged electrode is ~27% anhydrous NVO, ~23% monohydrate NVO, 16% ZHS and 36% ZVO (**Table S6**). Upon charge, the electrode composition consists of anhydrous NVO (61%), monohydrate NVO (13%) and ZVO (26%) (**Figure 7c**, **Figure S4b**, **Table S7**). ZHS was not detected in the XRD pattern after charging.

The phase composition of NVO(500) electrodes discharged to 0.4 V is ~61% anhydrous NVO, ~26% ZHS, and ~12% ZVO (**Figure 7e**, **Figure S4c**, **Table S8**). Upon charge to 1.4 V, NVO(500) electrodes consist of anhydrous NVO (77%) and ZVO (24%) (**Figure 7f**, **Figure S4d**, **Table S9**). ZHS was also not detected in the XRD pattern of NVO(500) electrodes after charging.

The ZHS is formed via precipitation due to generation of local OH^- indicating a H^+ insertion mechanism.²⁵ On charge, the ZHS phase is not detected, suggesting complete reversibility of H^+ insertion. In contrast, ZVO phase remains in the charged state, suggesting the formation of this phase is partially irreversible. The irreversibility of this phase is consistent with differences in cycle 1 and cycle 2 columbic efficiency observed for both NVO(300) and NVO(500) materials (**Figure 4**). Notably, the NVO(300) electrode has ~66% increased ZVO content relative to the NVO(500) electrode in the discharge state. Likewise, the NVO(500) electrode exhibits 37% more ZHS phase relative to NVO(300) electrodes in the discharged state.



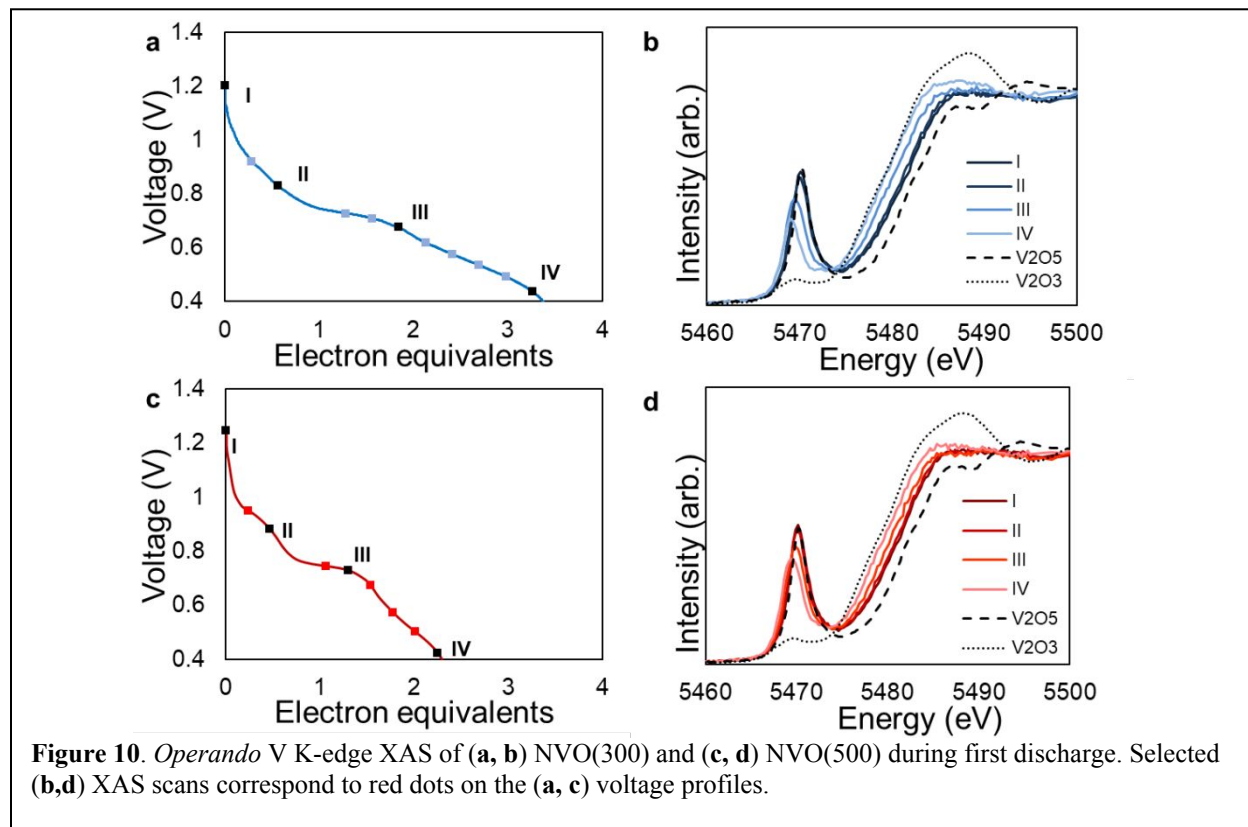
The structural changes of NVO(300) and NVO(500) were further characterized by TEM, HRTEM, SAED, and EDS maps. For NVO(300) (**Figure 8**), minor cracks mostly aligned along *b*-axis are observed upon cycle 1 discharge (**Figure 8b**) and charge (**Figure 8e**) from high-resolution TEM images. Additionally, the measured *c*-plane increases to 1.20 nm on cycle 1 discharge and returns to 1.18 nm on cycle 1 charge, analogous to the pristine material. The minor cracks and changes in *c*-plane spacing observed by HRTEM (**Figure 8b and e**) and the EDS maps (**Figure 8c and 8f**) upon cycle 1 discharge and charge suggest possible Zn insertion and extraction from the structure, consistent with identification of a ZVO phase in the XRD refinements.^{17, 34} A small amount of Zn ion remains within the structure after charge, indicating that Zn extraction was not completely reversible, consistent with the presence of ZVO in the bulk XRD pattern on charge and low cycle 1 Coulombic efficiency.



For NVO(500) (**Figure 9**), the *c*-plane spacing is consistent upon discharge and charge (1.15 nm), and there is no observable structural degradation, suggesting minimal Zn insertion. The EDS maps also show reduced Zn signal upon cycle 1 discharge relative to NVO(300) (**Figure 9c**) and minimal Zn signal upon cycle 1 charge (**Figure 9f**). The Zn signal at the surface of NVO(500) (**Figure 9c**)

is likely attributed to ZHS formation, and suggest delivered capacity may be dominated by a H^+ insertion mechanism. The reduced Zn content in the discharged NVO(500) material is consistent with the lower delivered capacities and currents observed during galvanostatic cycling and CV measurements, respectively relative to NVO(300).

Operando Characterization.



Vanadium K-edge XAS measurements were collected on NVO(300) and NVO(500) *operando* cells cycled galvanostatically from 0.4 V to 1.4 V vs. Zn/Zn^{2+} at 60 mA/g and 50 mA/g, respectively (**Figure 10**, **Figure S5**). Voltage profiles between the *operando* cells and coin cells are comparable (**Figure S6**). The XAS scans before and during cycling were compared to V_2O_5 , VO_2 , V_2O_3 reference materials to estimate the vanadium oxidation state from the absorption edge (**Figure S7**). Additionally, the position and intensity of the pre-edge peak was tracked as a function of electron equivalents to further probe changes in oxidation state and local atomic environment (**Figure 11**, **Figure 12**). NVO(300) and NVO(500) materials were incorporated into boron nitride pellets to determine the NVO atomic chemical and structural environment in the pristine state.

In the pristine state, NVO(300) has an intense pre-edge feature, associated with asymmetric VO_5 square pyramids, which exist in a 1:3 ratio with VO_6 octahedra (**Figure 1**). The strongly distorted VO_5 square pyramids have one shorter apical bond ($\sim 1.62 \text{ \AA}$) and four longer V-O bonds (~ 1.71 to 1.99 \AA), which result in broken symmetry and allow for V $3d-4p$ mixing and hybridization of V 3d with O $2p$ orbitals.³⁵⁻³⁷ The edge position is 5182.1 eV, consistent with the V_2O_5 reference material indicating the NVO(300) material originates as V^{5+} . The edge position of the NVO(300) electrode incorporated into the aqueous *operando* cell is 5479.9 eV, corresponding to a vanadium

oxidation state of ~ 4.3 when compared to the V_2O_5 , VO_2 , and V_2O_3 *ex-situ* standards (**Figure S7**). Comparison of the NVO(300) electrode in the *operando* cell before discharge to the pristine NVO(300) material suggests the vanadium reduces slightly in the cell environment containing the 2M $ZnSO_4$ electrolyte. During cycle 1 discharge at 50 mAh/g, the edge position decreases steadily and reaches 5477.7 eV at 0.4 V, which corresponds to an average vanadium oxidation state of 3.2. The decrease in the vanadium oxidation state from $V^{4.3+}$ to $V^{3.2+}$ is consistent with the delivered capacity on the first discharge (291 mAh/g, 3.3 ee). These results suggest that each electron equivalent transferred corresponds to a reduction of a vanadium center. Additionally, the pre-

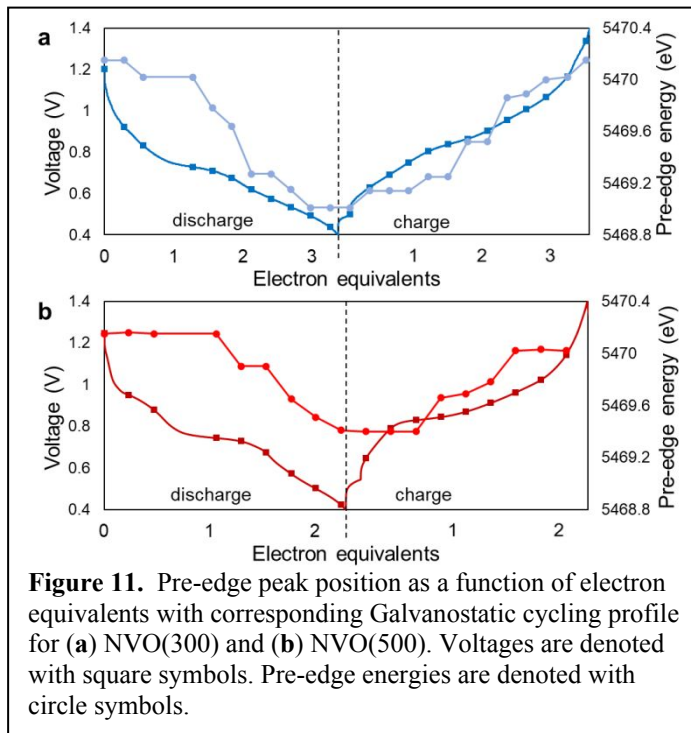


Figure 11. Pre-edge peak position as a function of electron equivalents with corresponding Galvanostatic cycling profile for (a) NVO(300) and (b) NVO(500). Voltages are denoted with square symbols. Pre-edge energies are denoted with circle symbols.

edge peak position (**Figure 11**) decreases from 4570.2 eV to 5469.0 eV and the pre-edge intensity also decreases during the discharge (**Figure 12a**). Decreases in vanadium pre-edge peak intensity have been observed during NaV_3O_8 electrochemical lithiation in non-aqueous electrolyte, associated with a progressive loss of crystalline character resulting in the formation of more regular octahedra.³⁸ Upon charge to 1.4 V (**Figure S5a, S5b**), the edge and pre-edge positions return to 5480.0 eV and 4570.2 eV, respectively suggesting a reversible oxidation to a 4.3 oxidation state.

In the pristine state, NVO(500) also exhibits an intense pre-edge feature and an edge position at 5182.1 eV, indicating the vanadium centers of the pristine material are V^{5+} . In the *operando* cell (**Figure 10c, 10d**), the edge position of NVO(500) is 5479.9 eV, consistent with an oxidation state of 4.3. During discharge, the edge position steadily decreases to 5478.1 eV at 0.4 V, corresponding to an oxidation state of 3.6, higher than the NVO(300) material. The decrease in the NVO(500) vanadium oxidation state from $V^{4.3+}$ to $V^{3.6+}$ is consistent with the delivered capacity observed on the first discharge (185 mAh/g, 2.1 ee). A decrease in the pre-edge peak position from 4570.2 eV to 5469.4 eV (**Figure 11b**) and a decrease in pre-edge peak intensity is also observed on first discharge (**Figure 12b**). Upon charge, the edge and pre-edge peak positions return to 5480.0 eV and 4570.2 eV, respectively; and the pre-edge peak intensity increases.

The *operando* XAS results of NVO(300) and NVO(500) indicate the vanadium reduction and oxidation is reversible and consistent with the delivered capacities observed in the electrochemistry. Additionally, both NVO(300) and NVO(500) demonstrate a decrease in the pre-edge peak intensity on discharge. The pre-edge peak intensity for NVO(300) decreases by 43% from the original intensity; whereas, the peak intensity decreases by 24% for NVO(500) consistent with the lower delivered capacity for the NVO(500) material. Notably, the ZVO discharge product $[Zn_3(OH_2)(V_2O_7)(H_2O)_2]$ observed via XRD and TEM consists of VO_4 tetrahedra. Vanadium centers with tetrahedral geometry commonly generate XAS spectra with more intense pre-edge

features relative to octahedral centers due to decreased symmetry.³⁹ Thus, the decrease in pre-edge intensity during discharge (**Figure 12**) is attributed to structural change of NaV_3O_8 , rather than $[\text{Zn}_3(\text{OH}_2)(\text{V}_2\text{O}_7)(\text{H}_2\text{O})_2]$ formation. In summary, NVO(300) delivers greater capacity on discharge and charge; and therefore, exhibits greater vanadium oxidation state change and greater amorphization relative to the NVO(500) analog.

Conclusion

In this work, NaV_3O_8 (NVO) was synthesized using a sol-gel method and calcined at 300°C [NVO(300)] or 500°C [NVO(500)] to form the materials for the study. XRD, TEM, SEM, TGA, and BET characterization of the NVO(500)

$[\text{NaV}_3\text{O}_8 \cdot 0.05\text{H}_2\text{O}]$ indicate that the higher annealing temperature of 500°C results in larger crystallite size, shorter and thicker nanorod particles, with reduced surface area and interlayer water content. In contrast, the annealing temperature of 300°C , results in a smaller crystallite size, longer and thinner nanobelt particles, higher surface area and water content for NVO(300) $[\text{NaV}_3\text{O}_8 \cdot 0.34\text{H}_2\text{O}]$. Notably, the water content of layered vanadates is important for aqueous batteries, as previous reports suggest interlayer water molecules may be key for increasing interlayer spacing to promote intercalation of ions. The *a*-plane interlayer spacing for NVO(300) and NVO(500) were 7.06 \AA and 6.98 \AA , respectively based on the powder x-ray diffraction pattern. NVO(300) and NVO(500) show distinct electrochemistry in zinc-ion aqueous cells. Cyclic voltammetry indicates NVO(300) has larger effective diffusion coefficients than NVO(500), consistent with the smaller crystallite size, larger surface area, larger interlayer spacing and thin nature of the nanobelts. Galvanostatic cycling and rate capability show NVO(300) cells deliver greater capacities at all tested rates; however, also show greater capacity decrease over extended cycling.

Ex-situ XRD and TEM and *operando* XAS were used to probe the charge storage mechanism in NVO(300) and NVO(500) zinc-ion aqueous cells. XRD and TEM show $\text{Zn}_4\text{SO}_4(\text{OH})_6 \cdot 5\text{H}_2\text{O}$ (ZHS) and zinc vanadium oxide ($\text{Zn}_3(\text{OH}_2)(\text{V}_2\text{O}_7)(\text{H}_2\text{O})_2$, ZVO) phases, in addition to NaV_3O_8 are present in the discharge state, which suggest H^+ and Zn^{2+} insert into the NVO(500) and NVO(300) materials. During charge, ZHS disappears while ZVO remains, suggesting H^+ insertion is reversible and some Zn^{2+} insertion is irreversible for both materials. Rietveld refinements show more ZVO product forms during discharge of NVO(300) relative to NVO(500), consistent with EDS maps and TEM images that show higher Zn intensities and increased *c*-plane spacing. In contrast, more ZHS forms during discharge of NVO(500) relative to NVO(300) and increase in *c*-plane spacing is not observed via TEM images. *Operando* XAS suggests each electron equivalent transferred during discharge of the NVO(300) and NVO(500) cells corresponds to reduction of a

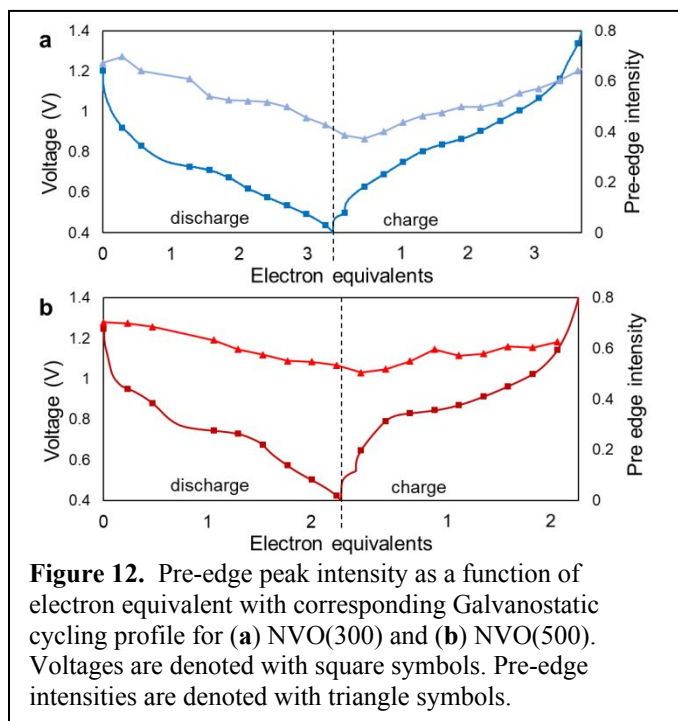


Figure 12. Pre-edge peak intensity as a function of electron equivalent with corresponding Galvanostatic cycling profile for (a) NVO(300) and (b) NVO(500). Voltages are denoted with square symbols. Pre-edge intensities are denoted with triangle symbols.

vanadium center. The NVO(300) cell delivers greater capacity (291 mAh/g, 3.3 ee); and therefore, has a lower average vanadium oxidation state ($V^{3.2+}$) at the end of discharge relative to NVO(500) ($V^{3.6+}$, 185 mAh/g, 2.1 ee). Vanadium oxidation state increases on charge to $V^{4.3+}$, which also correlates to charge capacity for both NVO(300) and NVO(500) cells.

This study shows that electrochemical properties of NVO materials in aqueous Zn-ion systems can be modified via variation in post-synthesis heat treatment, whereby characteristics such as crystallite size, particle size, interlayer water content, and surface area can be controlled. The lower temperature prepared NVO(300) yielded smaller crystallite size and larger surface area with a corresponding larger effective diffusion coefficient and improved delivered capacity at all rates. However, the NVO(300) material also yielded increased capacity fade over extended cycling. Thus, control of material properties via synthesis allows for control of the delivered capacity, rate capability and capacity retention of Zn-ion aqueous cells. Moreover, control of NVO material properties is shown to influence the relative amount and type of ion insertion (Zn^{2+} and H^+), an important factor for aqueous zinc-ion electrochemistry.

Conflict of Interest Statement

There are no conflicts of interest to declare.

Acknowledgement

Materials synthesis, characterization, cyclic voltammetry, and *operando* electrochemistry and characterization were supported by the Center for Mesoscale Transport Properties, an Energy Frontier Research Center supported by the DOE-BES, under Award #DE-SC0012673. Extended galvanostatic cycling and rate capability (as shown in Figure 6) were supported by the Department of Energy, Office of Electricity, administered through Sandia National Laboratories, Purchase Order #1955692. The XAS measurements used the NIST Beamline for Materials Measurement (BMM) 6-BM beamline at the National Synchrotron Light Source II, a U.S. Department of Energy (DOE) Office of Science User Facility operated for the DOE Office of Science by Brookhaven National Laboratory under Contract DE-SC0012704. C.R.T. acknowledges the support of the National Science Foundation Graduate Research Fellowship under Grant 1839287. Any opinions, findings, and conclusions or recommendations expressed in this material are those of the authors and do not necessarily reflect the views of the National Science Foundation. E.S.T. acknowledges funding from the William and Jane Knapp Chair for Energy and the Environment.

References

1. J. W. Choi and D. Aurbach, *Nature Reviews Materials*, 2016, **1**, 1-16.
2. L. M. Housel, W. Li, C. D. Quilty, M. N. Vila, L. Wang, C. R. Tang, D. C. Bock, Q. Wu, X. Tong, A. R. Head, K. J. Takeuchi, A. C. Marschilok and E. S. Takeuchi, *ACS Applied Materials & Interfaces*, 2019, **11**, 37567-37577.
3. T. N. Lambert, D. J. Davis, S. J. Limmer, M. R. Hibbs and J. M. Lavin, *Chem. Commun.*, 2011, **47**, 9597-9599.
4. L. Fan, Y. Ru, H. G. Xue, H. Pang and Q. Xu, *Advanced Sustainable Systems*, 2020, **4**.

5. Z. X. Liu, H. M. Sun, L. P. Qin, X. X. Cao, J. Zhou, A. Q. Pan, G. Z. Fang and S. Q. Liang, *Chemnanomat*, 2020, **6**, 1553-1566.
6. S. Y. Zuo, X. J. Xu, S. M. Ji, Z. S. Wang, Z. B. Liu and J. Liu, *Chemistry-a European Journal*, DOI: 10.1002/chem.202002202.
7. V. Augustyn, P. Simon and B. Dunn, *Energy & Environmental Science*, 2014, **7**, 1597-1614.
8. C. G. Li, X. D. Zhang, W. He, G. G. Xu and R. Sun, *Journal of Power Sources*, 2020, **449**.
9. F. Wan and Z. Q. Niu, *Angewandte Chemie-International Edition*, 2019, **58**, 16358-16367.
10. Z. Peng, Q. Wei, S. Tan, P. He, W. Luo, Q. An and L. Mai, *Chem. Commun.*, 2018, **54**, 4041-4044.
11. B. Tang, G. Fang, J. Zhou, L. Wang, Y. Lei, C. Wang, T. Lin, Y. Tang and S. Liang, *Nano Energy*, 2018, **51**, 579-587.
12. B. Tang, J. Zhou, G. Fang, F. Liu, C. Zhu, C. Wang, A. Pan and S. Liang, *Journal of Materials Chemistry A*, 2019, **7**, 940-945.
13. Z. Xie, J. Lai, X. Zhu and Y. Wang, *ACS Appl. Energy Mater.*, 2018, DOI: 10.1021/acsaem.8b01378, Ahead of Print.
14. N. Qiu, Z. Yang, Y. Wang, Y. Zhu and W. Liu, *Chem. Commun.*, 2020, **56**, 9174-9177.
15. W.-J. Kwak, Rosy, D. Sharon, C. Xia, H. Kim, L. R. Johnson, P. G. Bruce, L. F. Nazar, Y.-K. Sun, A. A. Frimer, M. Noked, S. A. Freunberger and D. Aurbach, *Chemical Reviews*, 2020, **120**, 6626-6683.
16. X. Shen, Y. Li, T. Qian, J. Liu, J. Zhou, C. Yan and J. B. Goodenough, *Nature Communications*, 2019, **10**, 900.
17. P. He, G. Zhang, X. Liao, M. Yan, X. Xu, Q. An, J. Liu and L. Mai, *Advanced Energy Materials*, 2018, **8**, 1702463.
18. X. Guo, G. Fang, W. Zhang, J. Zhou, L. Shan, L. Wang, C. Wang, T. Lin, Y. Tang and S. Liang, *Advanced Energy Materials*, 2018, **8**, 1801819.
19. V. Soundharrajan, B. Sambandam, S. Kim, M. H. Alfaruqi, D. Y. Putro, J. Jo, S. Kim, V. Mathew, Y.-K. Sun and J. Kim, *Nano Letters*, 2018, **18**, 2402-2410.
20. F. Wan, L. Zhang, X. Dai, X. Wang, Z. Niu and J. Chen, *Nat Commun*, 2018, **9**, 1656.
21. F. Hu, D. Xie, D. P. Zhao, G. H. Song and K. Zhu, *J. Energy Chem.*, 2019, **38**, 185-191.

22. S. Islam, M. H. Alfaruqi, B. Sambandam, D. Y. Putro, S. Kim, J. Jo, S. Kim, V. Mathew and J. Kim, *Chemical Communications*, 2019, **55**, 3793-3796.
23. P. Hu, T. Zhu, X. Wang, X. Wei, M. Yan, J. Li, W. Luo, W. Yang, W. Zhang, L. Zhou, Z. Zhou and L. Mai, *Nano Letters*, 2018, **18**, 1758-1763.
24. X. Zhang, Y. Zhu, A. M. Bruck, L. M. Housel, L. Wang, C. D. Quilty, K. J. Takeuchi, E. S. Takeuchi, A. C. Marschilok and G. Yu, *Energy Storage Materials*, 2019, **19**, 439-445.
25. X. Shan, S. Kim, A. M. M. Abeykoon, G. Kwon, D. Olds and X. Teng, *ACS Applied Materials & Interfaces*, 2020, **12**, 54627-54636.
26. S. J. Kim, C. R. Tang, G. Singh, L. M. Housel, S. Yang, K. J. Takeuchi, A. C. Marschilok, E. S. Takeuchi and Y. Zhu, *Chemistry of Materials*, 2020, DOI: 10.1021/acs.chemmater.9b05103.
27. B. H. Toby and R. B. J. J. o. A. C. Von Dreele, 2013, **46**, 544-549.
28. M. Onoda, *Journal of Physics: Condensed Matter*, 2004, **16**, 8957.
29. H. G. Bachmann and W. H. Barnes, *The Canadian Mineralogist*, 1962, **7**, 219-235.
30. C. A. Schneider, W. S. Rasband and K. W. Eliceiri, *Nature Methods*, 2012, **9**, 671-675.
31. B. Ravel and M. Newville, *Journal of synchrotron radiation*, 2005, **12**, 537-541.
32. B. Ravel and M. Newville, *Physica Scripta*, 2005, **2005**, 1007.
33. M. Onoda, *J. Phys.-Condes. Matter*, 2004, **16**, 8957-8969.
34. J. Meng, Z. Liu, C. Niu, X. Xu, X. Liu, G. Zhang, X. Wang, M. Huang, Y. Yu and L. Mai, *Journal of Materials Chemistry A*, 2016, **4**, 4893-4899.
35. G. A. Horrocks, E. J. Braham, Y. Liang, L. R. De Jesus, J. Jude, J. M. Velázquez, D. Prendergast and S. Banerjee, *The Journal of Physical Chemistry C*, 2016, **120**, 23922-23932.
36. J. Wong, F. W. Lytle, R. P. Messmer and D. H. Maylotte, *Physical Review B*, 1984, **30**, 5596-5610.
37. M. Giorgetti, S. Passerini, W. H. Smyrl, S. Mukerjee, X. Q. Yang and J. McBreen, *J. Electrochem. Soc.*, 1999, **146**, 2387-2392.
38. R. Tossici, R. Marassi, M. Berrettoni, S. Stizza and G. Pistoia, *Solid State Ionics*, 1993, **67**, 77-83.
39. T. Yamamoto, *X-Ray Spectrometry*, 2008, **37**, 572-584.